The Astrophysical Journal, 738:127 (13pp), 2011 September 10 doi:10.1088/0004-637X/738/2/127

NUMERICAL INVESTIGATION OF A CORONAL MASS EJECTION FROM AN ANEMONE ACTIVE REGION: RECONNECTION AND DEFLECTION OF THE 2005 AUGUST 22 ERUPTION

N. Lugaz[1,2], C. Downs[2], K. Shibata[1], I. I. Roussev[2], A. Asai[3], and T. I. Gombosi[4]
[1] Kwasan Observatory, Kyoto University, Kyoto, Japan
[2] Institute for Astronomy, University of Hawaii, Honolulu, HI, USA
[3] Unit of Synergetic Studies for Space, Kyoto University, Kyoto, Japan
[4] Center for Space Environment Modeling, University of Michigan, MI, USA
Received 2011 April 7; accepted 2011 June 16; published 2011 August 18

ABSTRACT

We present a numerical investigation of the coronal evolution of a coronal mass ejection (CME) on 2005 August 22 using a three-dimensional thermodynamic magnetohydrodynamic model, the space weather modeling framework. The source region of the eruption was anemone active region (AR) 10798, which emerged inside a coronal hole. We validate our modeled corona by producing synthetic extreme-ultraviolet (EUV) images, which we compare to EIT images. We initiate the CME with an out-of-equilibrium flux rope with an orientation and chirality chosen in agreement with observations of an Hα filament. During the eruption, one footpoint of the flux rope reconnects with streamer magnetic field lines and with open field lines from the adjacent coronal hole. It yields an eruption which has a mix of closed and open twisted field lines due to interchange reconnection and only one footpoint line-tied to the source region. Even with the large-scale reconnection, we find no evidence of strong rotation of the CME as it propagates. We study the CME deflection and find that the effect of the Lorentz force is a deflection of the CME by about 3° $R_\odot^{-1}$ toward the east during the first 30 minutes of the propagation. We also produce coronagraphic and EUV images of the CME, which we compare with real images, identifying a dimming region associated with the reconnection process. We discuss the implication of our results for the arrival at Earth of CMEs originating from the limb and for models to explain the presence of open field lines in magnetic clouds.

Key words: magnetohydrodynamics (MHD) – Sun: corona – Sun: coronal mass ejections (CMEs) – Sun: magnetic topology

Online-only material: animations, color figures

1. INTRODUCTION

Coronal mass ejections (CMEs) are one of the leading causes of space weather, especially when they have organized southward-directed magnetic fields. Therefore, it is of great importance for space weather forecasting to understand how their direction of propagation and their orientation at 1 AU relate to properties on the solar disk (location of source region, orientation of the polarity inversion line, etc.). The deflection of CMEs in the latitudinal direction has been observed and reported since the launch of the first space coronagraphs in the 1970s and 1980s. For example, MacQueen et al. (1986) reported an average deflection of $2\overset{\circ}{.}2$ toward the equator for 29 CMEs during solar minimum (1973–1974), while they found no systematic deflection for 19 CMEs during solar maximum (1980). With the launch of the *Solar–Terrestrial Relations Observatory* (*STEREO*) in 2006, there has been a renewed focus on the deflection of CMEs in the corona and the heliosphere, thanks to stereoscopic measurements from the two spacecraft (e.g., see Kilpua et al. 2008; Liu et al. 2010; Byrne et al. 2010).

The presence of coronal holes is known to affect the direction of propagation of CMEs (Plunkett et al. 2001; Gopalswamy et al. 2009). However, the exact cause of this influence is uncertain. Cremades et al. (2006) and Gopalswamy et al. (2009) have used an ad hoc, fictitious force exercised by coronal holes on CMEs, which is directly dependent on the coronal hole area and the distance of the CME source region from the coronal hole. This force might be due to a "pushing" of the CME by the fast wind from the coronal hole (Wang et al. 2004). Plunkett et al. (2001) proposed that the effect of coronal holes is due to strong magnetic fields, Filippov et al. (2001) proposed that the non-radial motion is due to the guiding action of the coronal magnetic field, while Aulanier et al. (2010) and Shen et al. (2011) recently proposed that magnetic pressure gradient acting on a CME results in a net force directed along the gradient of the magnetic pressure. Obviously, magnetic forces, such as the Lorentz force could also cause the coronal hole to exercise a force on the CME. Magnetic forces are expected to affect strongly the evolution and propagation of a CME in the corona while the effect of the fast solar wind from the coronal hole would continue into the heliosphere and be more gradual.

Similar effects may result in the rotation of an eruption. One of the leading causes of CME rotation is the kink instability (Török & Kliem 2003) but recent numerical efforts have focused on other sources of rotation, such as reconnection with the background magnetic field (Cohen et al. 2010), the effect of the Lorentz force (Isenberg & Forbes 2007; Shiota et al. 2010), and its association with shearing motions (Lynch et al. 2009). These numerical works point toward a near universal rotation for CMEs not initially aligned with the heliospheric current sheet (HCS). While statistically speaking, CMEs rotate toward the HCS (Yurchyshyn 2008), it appears from observations that some CMEs do not rotate, even though they are originally not aligned with the HCS (see some cases in Yurchyshyn 2008; Yurchyshyn et al. 2009).

Eruptions from ARs which are inside a coronal hole present a perfect configuration to study the effect of coronal holes on CMEs. For example, the fictitious force of Cremades et al. (2006) is inversely proportional to the square of the distance between the source region and the coronal hole, and it results in

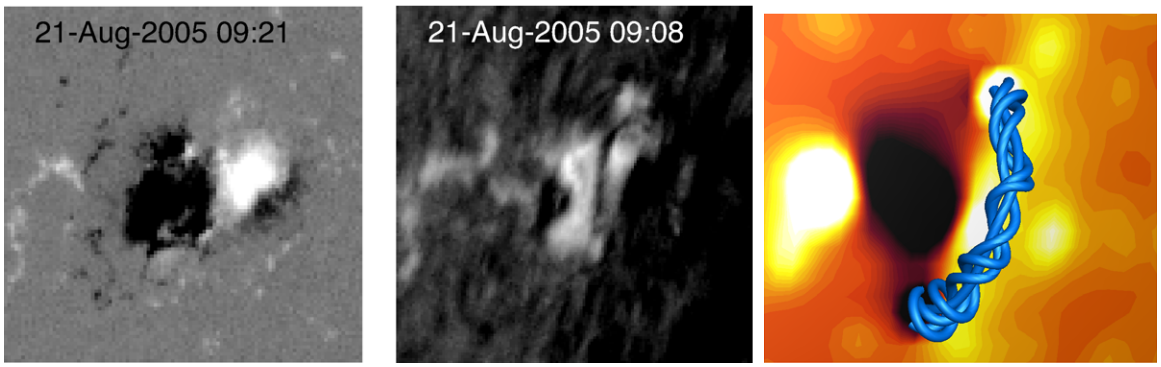

Figure 1. Initial configuration of the filament. Left: *SOHO*/MDI magnetogram. Middle: Hα image of the filament taken at the Observatoire de Paris–Meudon. Right: MHD simulation at time $t = 0$ with the background magnetic field on the solar surface and the flux rope shown with blue field lines. In all three views, the images show approximately 200 arcsec × 200 arcsec.

(A color version of this figure is available in the online journal.)

an infinite force for a CME originating from such an AR. ARs can form inside coronal holes and, then, they often develop into anemone ARs (Shibata et al. 1994; Asai et al. 2008). Anemone ARs were originally observed in soft X-ray (SXR) and named X-ray fountains (Sheeley et al. 1975) due to the structure looking like a fountain with loops emerging in all directions from the center. Almost identical structures are observed in extreme-ultraviolet (EUV) and in chromospheric lines (Shibata et al. 2007). In a survey of ARs observed by the Soft X-ray Telescope (see Tsuneta et al. 1991) on board *Yohkoh* (Ogawara et al. 1991), Asai et al. (2008) found that as many as 25% of ARs observed in 1991–1992 appeared as anemone ARs at one time during their evolution, and that there is a near equivalence between an AR having an anemone structure and being inside a coronal hole.

Anemone ARs have been primarily studied as the source of X-ray jets since the emergence of a bipolar AR inside unipolar open magnetic fields naturally yield such phenomena (Shibata et al. 1994; Vourlidas et al. 1996). Of greater importance for space weather are the instances of CMEs and filament eruptions from anemone ARs (Chertok et al. 2002; Asai et al. 2009; Baker et al. 2009). Liu (2007) found that eruptions from ARs inside open magnetic fields (which contain anemone ARs) are statistically faster on average than other eruptions (even originating from under the HCS). Most authors have explained this result by invoking two facts. Since the eruption originates from a region of low-density, fast solar wind, the fast wind can "push" the CMEs to a faster speed. Closed field in the low corona (LC) can hinder the eruption of the CME because of the Lorentz force (see, for example, the model of Chen 1996) and in the absence of closed field lines, the CME can erupt without being strongly decelerated.

In the present work, we investigate the effect of the particular magnetic structure of anemone ARs on the evolution and coronal propagation of a CME. We focus on the first of two eruptions on 2005 August 22 from AR NOAA 10798. This CME was associated with the eruption of a southward-directed Hα filament and reached a speed of about 1200 km s^{-1} (for a complete overview of the observations, see Asai et al. 2009). The second eruption was faster ($\sim$2400 km s^{-1}) and it occurred about 16 hr after the first one from the same AR. The eruption of a preceding CME from the same AR is expected to significantly change the magnetic topology of the source region (Lugaz et al. 2010) and also modify the background solar wind into which the second CME propagates (Lugaz et al. 2005, 2007), which would complicate a numerical investigation of the second CME. For this reason, we focus on the first CME. Our investigation is based on a numerical magnetohydrodynamic (MHD) model, part of the space weather modeling framework (SWMF; see Tóth et al. 2005). In order to validate our simulation with EUV observations and to reproduce more accurately the lower part of the corona, we use the LC model recently developed by Downs et al. (2010), which captures the energy balance of the coronal plasma.

The organization of the paper is as follows. In Section 2, we briefly summarize the main features of the LC and flux rope models important for this study. Then, we discuss the magnetic topology of the anemone AR before presenting a comparison of the pre-event corona as observed in EUV with the modeled corona in synthetic EUV. In Section 3, we follow the initial phases of the eruption and explain its interaction with the adjacent magnetic flux systems. In this section, we also discuss the CME aspect in real and synthetic coronagraphic images. We study the CME rotation, deformation, and deflection in Section 4. We discuss our results and conclude in Section 5.

2. NUMERICAL MODELS AND PRE-EVENT MODELING

2.1. Low Corona Model

The simulation is done using the LC component of the SWMF. The LC model includes radiative losses, field-aligned electron heat condition, and empirical heating terms in the energy equation as detailed in Downs et al. (2010). It has been recently used to study the nature of the EUV wave observed by the two *STEREO* spacecraft on 2008 March 25 (Downs et al. 2011). The initial magnetic field and boundary conditions are provided by a finite difference solution of the potential field source surface method (Altschuler et al. 1977) for the synoptic magnetogram of Carrington rotation 2033 as observed by the *Solar and Heliospheric Observatory*/Michelson Doppler Imager (*SOHO*/MDI) instrument (Tóth et al. 2011). As noted in Asai et al. (2009), AR 10798 was rapidly evolving as it crossed the Sun central meridian and therefore, the synoptic map does not fully capture the complexity of the AR as revealed by observations on August 21 and 22. However, on these two days, the AR was already too close to the eastern limb of the Sun, so that the daily line-of-sight magnetogram (shown in the left panel of Figure 1) cannot be adequately used to constrain our model. As discussed below, even using the synoptic map, the MHD model successfully reproduces the important features of the anemone AR.

As described in Downs et al. (2010), we followed the previous work of Lionello et al. (2001, 2009) to widen the transition

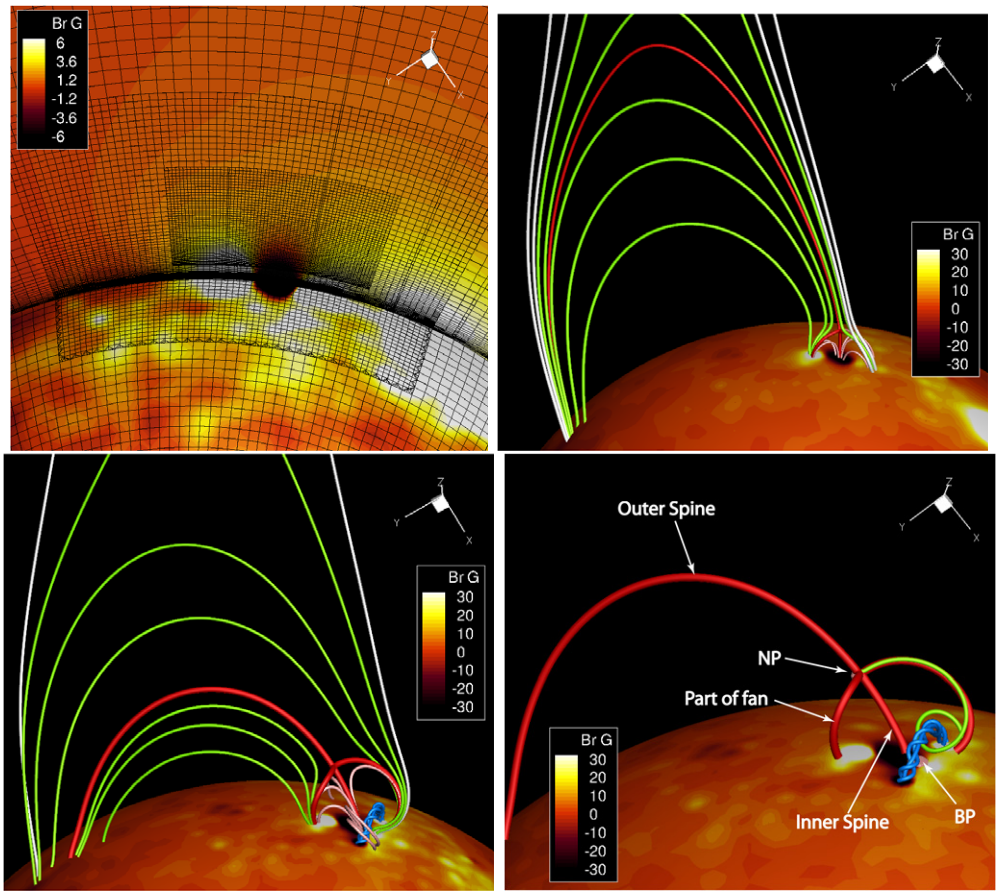

Figure 2. Initial configuration of the corona around AR 10798 from the simulation with the grid structure (top left), the anemone structure of the active region before the inclusion of the flux rope (top right), and after (bottom panels). White, green, pink, and blue field lines show open, streamer, active region, and flux rope magnetic field, respectively. The solar surface is color-coded with the radial magnetic field strength. The bottom right panel shows the zoomed version of the flux rope as it is added to the solar surface with a view of the bald patch (BP) and the null point (NP) as pink isosurfaces. In red, we show the inner and outer spines of the system as well as one of the field lines of the fan surface.

(A color version of this figure is available in the online journal.)

region by modifying the ratio of heat conduction to radiative cooling at temperatures below 300,000 K. The heating model and boundary conditions are the same as the ones described in Downs et al. (2011), i.e., we use the chromospheric boundary conditions. The grid is spherical with non-uniform radial scales near the transition region (minimum uniform $dr \sim 230$ km) with a resolution on the solar surface of $1.^{\circ}4 \times 1.^{\circ}4$. In addition, we further refine around AR 10798 by two levels of refinement as follows. The solar surface is refined twice in a box of about 20° latitude and 40° longitude around the AR over a height of 0.4 $R_{\odot}$ and the region around the top of the anemone structure (null point, NP) is refined by an additional factor of two in a twice smaller box centered at 1.15 $R_{\odot}$, resulting in a smallest angular resolution of $0.^{\circ}35 \times 0.^{\circ}35$. The grid around AR 10798 is shown in the top left panel of Figure 2.

This version of the LC model includes a uniform Parker-like solar wind model but not a bimodal solar wind model as in the models of Cohen et al. (2007) and van der Holst et al. (2010). Here, the solar wind accelerates and becomes faster than the fast magnetosonic speed between 6 and 14 $R_{\odot}$ and reaches a value of 300–350 km s^{-1} at the outer boundary of the domain (24 $R_{\odot}$). While it is not realistic for the fast wind originating from coronal holes, it is the approximate speed and acceleration profile expected for the slow solar wind. We only focus on the coronal evolution of the CME, therefore resolving a bimodal solar wind is not critical to our study. Since the solar wind is uniform, we can expect a negligible amount of deflection and rotation due to hydrodynamical effect (velocity shear, non-uniform drag). It allows us to focus solely on the effect of magnetic forces and reconnection on the CME evolution. Compared to previous studies of the evolution of CMEs in the corona with the SWMF (Lugaz et al. 2007; Cohen et al. 2010; Evans et al. 2011), using the LC model has a number of advantages. The inclusion of the thermodynamics makes the treatment of the lower corona more realistic. Using the chromospheric boundary conditions, the density and temperature of the plasma are based solely on the magnetic topology and the particular choice of heating function. Also, as discussed in Downs et al. (2010), it results in a less potential steady-state solution for the background coronal magnetic field. Finally, it gives us the opportunity to validate our model with a direct comparison to EUV observations.

2.2. CME Model

To model the CME, we employ a semi-circular flux rope prescribed by a given total toroidal current, as in the models by Titov & Démoulin (1999) and Roussev et al. (2003). An azimuthal current is also added at the surface of the flux rope in order to construct a force-free magnetic field inside the flux rope. The toroidal current is largely dominant, creating a very highly twisted flux rope. A more complete description of this implementation of the flux rope model can be found in Lugaz et al. (2007) and Evans et al. (2011). Because in this version

of the Titov & Démoulin (1999) flux rope, there is neither sub-surface line current nor sub-surface magnetic charges to generate strapping field for the flux rope in the corona, the flux rope is not expected to rotate as found for example in Isenberg & Forbes (2007). Additionally, the flux rope is constructed so that it is not kink unstable. The flux rope solution once superimposed onto the coronal magnetic field leads to an immediate eruption because of force imbalance with the ambient magnetic field.

A filament was observed on August 21 (see the middle panel of Figure 1) and the eruption of the northern section of the filament was the cause of the studied eruption (Asai et al. 2009). We place the flux rope at a position and with an orientation in agreement with the observation of the filament (see Figure 1). The flux rope (and the line current inside) makes an angle of -15° with the $-z$-axis (the Sun rotation axis). It results in a right-handed flux rope with an axial southward magnetic field, in agreement with the observations of the filament in Hα and with the reconstruction of the associated ejecta at 1 AU (Asai et al. 2009). The flux rope is making an angle of about 20° with the polarity inversion line of AR 10798 with its negative (resp. positive) footprint in the main part of the negative (resp. positive) polarity spot of the AR. The direction of the axial field of the flux rope is chosen in agreement with the observations of a southward (sinistral) filament (Asai et al. 2009) which is also consistent with the prefilament structure (see Figure 4 from Asai et al. 2009). The orientation of the axis of the flux rope is consistent with the observations of a structure oriented from the northwest to the southeast. The exact orientation is chosen so that the positive (resp. negative) footprint of the flux rope is in a region of positive (resp. negative) polarity, while the axis of the flux rope remains close to the polarity inversion line. It should be noted that in our MHD model, because we use a synoptic magnetogram, the positive polarity spot of the AR (on the west side of the negative spot) is not yet fully developed while the positive polarity on the east side is stronger that it is on August 21–22. The flux rope is chosen as right-handed to agree with the overall magnetic field in the overlying arcades once the direction of the axial field (sinistral) of the flux rope is chosen. This is also consistent with what was reported in Asai et al. (2009). Finally, the amount of twist is determined by the prescribed toroidal current. The current is set by a trial-and-error procedure to match the coronal speed of the CME as observed by LASCO (1200 km s^{-1}). Because of the way our flux rope is created (with a dominant toroidal current), the chosen value of the current results in a flux rope with a much larger amount of twist as compared to what is derived from observations (see review by Mackay et al. 2010).

Previous time-dependent simulations with the LC model were performed with the CME initiation model of Roussev et al. (2007). Here, we use, for the first time, a flux rope model in the LC model because the presence of a filament strongly suggests that a flux rope was present prior to the eruption. This CME model has been used before to study the evolution of CME in the corona (Lugaz et al. 2007; Cohen et al. 2010; Evans et al. 2011). A view of the flux rope at time $t = 0$ as it is superposed onto the steady-state corona is shown with blue field lines in the bottom panels of Figure 2.

2.3. Pre-event Topology

The magnetic topology before the eruption is very important because it determines, to a great extent, the location of the reconnection of the flux rope with adjacent magnetic field structures during the eruption. The steady-state corona around AR 10798 is relatively simple with (1) a large-scale streamer connecting the AR with a region of the quiet Sun about 40° east of the AR, (2) open field lines with positive polarity, and (3) AR closed field lines. We found no magnetic connectivity between AR 10798 and adjacent AR, even though AR 10797 is only about 20°–25° away. It is not surprising since AR 10798 is a reverse polarity AR (negative–positive), while AR 10797 follows the Hale et al. (1919) polarity law (positive–negative). Therefore, the positive parts of ARs 10798 and 10797 are next to each other and, moreover, they are embedded into positive polarity open magnetic fields from the coronal hole. This type of magnetic field configuration makes it very unlikely that there was a direct magnetic connectivity between these two ARs. The topology is much simpler than other cases near solar maximum, where Roussev et al. (2007) found connectivity between as many as three ARs via multiple NPs and quasi-separatrix layers.

There is one NP above the negative polarity part of AR 10798 separating the three flux systems as illustrated in Figure 2: AR field (pink), streamer field (green), and open field (white). Because the negative polarity spot is surrounded by positive polarities, it develops into an anemone AR (see the top right panel of Figure 2) as described before in Asai et al. (2008) and Shibata et al. (2007). This NP is originally at a height of 0.09 $R_\odot$ above the solar surface. This value is probably lower than that on the Sun at the time of the eruption because we use a synoptic map of the Sun and AR 10798 was not fully developed. The existence of close field lines as part of a unipolar region has been reported before (Chertok et al. 2002). The steady-state configuration is an embedded dipole, identical to that of the asymmetrical breakout model (Lynch et al. 2009) and similar to that of coronal jet studies (e.g., see Pariat et al. 2009) but with a closed outer spine. Here, the inner and outer spines are initially closed and there is a simple fan surface around the negative polarity spot of the AR. The inner and outer spines as well as one of the lines of the fan surface are shown in red in Figure 2. As we superpose the flux rope onto the AR, the NP is pushed by about 4° toward the northeast and by 0.04 $R_\odot$ upward, but the AR retains its anemone structure (see bottom panels of Figure 2). In addition, a bald patch (BP) forms below the flux rope (see bottom panels of Figure 2). Because AR 10798 develops and maintains its anemone structure in the simulation as was observed on the Sun, we believe our model captures the most important features of the solar corona before the 2005 August 22 eruptions.

2.4. Pre-event Comparison of the Simulated Corona with EUV Images

One of the advantages of using the LC model is the ability to simulate EUV images following the procedure described in Downs et al. (2010). It allows us to validate our steady-state model by comparing synthetic images with real ones prior to the event. The EUV signal depends on the density and temperature of the plasma and it is greatly influenced by the magnetic structure of the lower corona. Therefore, this type of comparisons validates not only the plasma properties of our simulated corona but also its detailed magnetic structure. We show a comparison of 195 Å and 171 Å images from the EUV Imaging Telescope (EIT; see Delaboudinière et al. 1995) on board *SOHO* 18 hr before the eruption with synthetic images for the same filters from our simulation in Figure 3. Synthetic and real images are plotted using the same scale. The 195 Å filter response function peaks around 1.4 MK, while the 171 Å peaks around 1 MK, illustrating different heights in the corona.

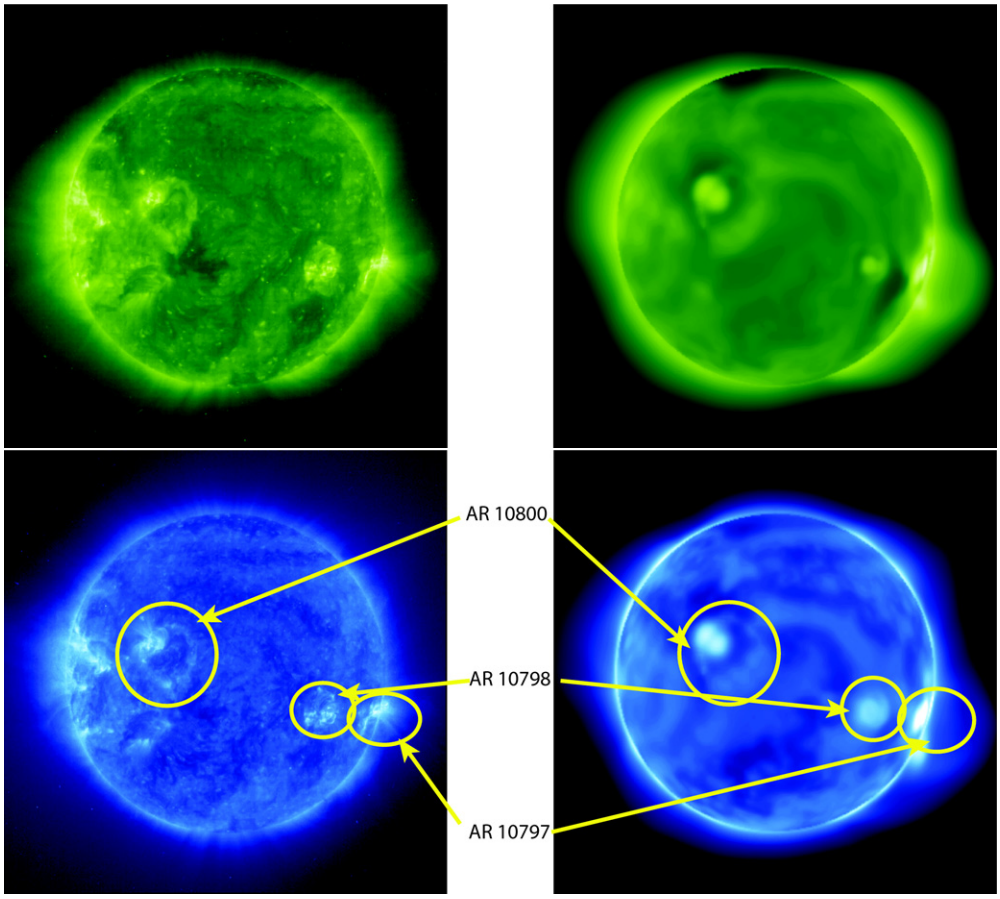

Figure 3. Real (left) and synthetic (right) EIT 195 Å image (top) and 171 Å image (bottom) of the corona 18 hr before the start of the first 2005 August 22 eruption and from our steady-state simulated corona. On the 171 Å images, the main active regions (ARs) are pointed out in yellow ellipses.
(A color version of this figure is available in the online journal.)

In synthetic and real images, the three ARs are clearly visible as regions of enhanced emission (hot and dense): the large AR 10800 on the eastern side of the Sun near disk center, AR 10797 near the western limb, and AR 10798 near W50. In addition to the northern polar coronal hole, there are a number of equatorial coronal holes, including two on the southwestern side of ARs 10798 and 10800. The southern polar coronal hole is almost absent in the simulated and real images. Overall, there is good agreement between synthetic and real images, which gives us confidence that our model of the corona is a relatively realistic representation of the actual corona at the time of the 2005 August 22 eruption. The most important features for our study that the model reproduces are the appearance of AR 10798 and the presence and aspect of open field regions (dark) around it. The main difference between simulated and real images is the eastern limb of the Sun where the modeled emission is too weak as compared to the real one. This is relatively unimportant because these regions are far from the source region of the CME (more than 120° separation) and are not involved in the eruption process.

3. CME EVOLUTION

3.1. Early Dynamics of the CME

As soon as we superpose the flux rope onto the steady-state coronal magnetic field, it erupts due to force imbalance. As in other simulations with the same CME model, the exact kinematics of the CME early on in the corona are not realistic as the CME reaches its maximum speed (∼1500 km s^{-1}) about 1.5 minutes after the superposition of the flux rope. However, the simulated CME kinematics past 3 $R_\odot$ (after 15 minutes) are in good agreement with the height–time profile as observed in LASCO/C2. Additionally, the CME speed after 1 hr is about 1200 km s^{-1}, similar to what is measured with LASCO (∼1250 km s^{-1}). It confirms that the total energy of the simulated CME is comparable to that of the real CME. The model does not intend to capture the slow rise phase before the loss of equilibrium nor the acceleration phase. This is why when comparing synthetic and real images, it is best not to use the onset time of the flare as the starting time of the numerical simulation but a later time when the CME has already significantly accelerated. Previous studies have found that the CME acceleration happens during the X-ray rise phase (Ohyama & Shibata 1998; Forbes 2000; Temmer et al. 2008). We use GOES-12 (Hill et al. 2005) and *RHESSI* (Lin et al. 2002) data to investigate the flare time in SXR and hard X-ray (HXR), respectively. For the ejection, the flare onset in SXR was 00:44UT, the HXR flare started at 01:02UT, and the flare peaked at 01:22UT. We believe the onset of the HXR flare is the best time to use for the start time of our simulation since the CME was already observed by LASCO at 4 $R_\odot$ 10 minutes after the flare peak.

Figure 4 shows a line-of-sight image of the CME observed by LASCO/C2 and processed with the method of Morgan et al. (2006) and a synthetic line-of-sight image from our simulation. The LASCO image is taken at 01:54 UT, 52 minutes after the

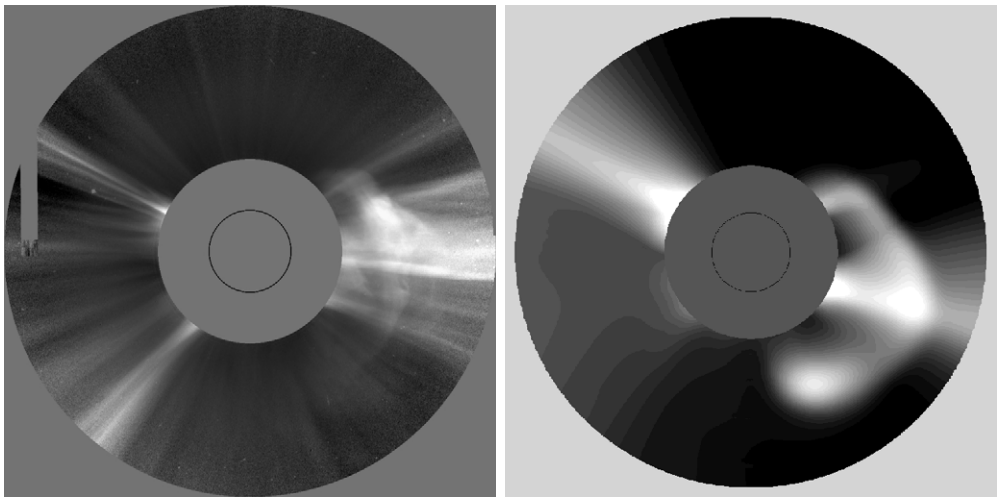

Figure 4. Line-of-sight image of the CME from LASCO/C2. The left panel is a real image 52 minutes after the start of the HXR flare and processed with the normalized radial gradient filter (NRGF; see Morgan et al. 2006). The right panel is a simulated image at time $t = 45$ minutes after the superposition of the flux rope onto the solar surface. A simulated 27 day minimum image is subtracted and the signal further scaled with distance.

onset of the HXR flare, while the synthetic image is made 45 minutes after the superposition of the flux rope onto the solar surface. The synthetic image is processed as explained in Lugaz et al. (2009) using a synthetic 27 day minimum image created from the steady-state simulation. The main difference between the synthetic and real images is the latitudinal direction of propagation of the CME. In the synthetic image, the fastest moving part of the CME is at a position angle (P.A.) of 210° while it is about 220°–225° for the real image (this region is dimmer than the main part of the CME which is closer to P.A. 270°). Because the CME appears as a halo, it is not straightforward to determine its central P.A. but the synthetic image shows a CME propagating about 15°–20° more toward the south as what appears in the real image. The AR was at the Carrington latitude South 11 (S11) when the ejection occurred and in our simulation, the CME propagates without a north–south deflection, i.e., along a latitude of S11. As noted in Asai et al. (2009), only the northern part of the filament erupted during the flare/ejection studied here, while the southern part erupted during the second CME on August 22. It is therefore likely that the real CME propagated more toward the north than what our simulation shows since only part of the filament erupted. With our relatively simple model to start the eruption, it is not yet possible to study partial filament eruptions.

As it rises and expands, the flux rope interacts and reconnects with the adjacent magnetic flux systems. Because this is a numerical study with finite resolution and based on numerical diffusion, the timing of the reconnection might not be realistic in our simulation. However, we believe that the reconnection process itself reflects what occurred on the Sun. It is because (1) our steady-state corona is a good representation of the pre-event Sun (see the previous section), (2) the CME was due to a filament, which was originally at approximately the same position with a similar length, and with the same orientation as our flux rope, and (3) the CME kinematics are in good agreement with what was observed by LASCO, meaning that the total energy in the flux rope is similar to that of the CME. In the section below, we analyze the interaction of the flux rope with the corona and in Section 3.4, we present some observational consequences of the reconnection process, which further validate the discussed scenario.

3.2. Reconnection of the Negative Footpoint

Only a few recent numerical works have focused on the interaction of a CME with a realistic magnetic structure obtained from magnetogram measurements (Roussev et al. 2007; Lugaz et al. 2010; Cohen et al. 2010; Evans et al. 2011). Other simulations have usually relied on an ideal representation of the corona with a single dipolar or quadrupolar AR in a dipolar Sun (as in Manchester et al. 2004b; Lynch et al. 2009; Jacobs et al. 2009; Shiota et al. 2010, for example). Here, the interaction of the flux rope with the background magnetic field is different from both these ideal cases and the realistic cases previously studied because of the anemone nature of the AR. The topology is different from the solar minimum cases studied before with an isolated AR not surrounded by equatorial coronal holes (Cohen et al. 2010; Evans et al. 2011) and also different from the two solar maximum case studies of Roussev et al. (2007) and Lugaz et al. (2010) with complex connectivity between multiple ARs. Recently, Titov et al. (2008) studied in great detail the magnetic topology of the corona before and during the evolution phase leading to the 1997 May 12 CME. Their study was also for a relatively simple magnetic topology without influence from equatorial coronal holes.

The evolution of the CME is altered by the anemone nature of the AR, i.e., by the presence of unipolar magnetic field around it. We find that the positive footpoint of the flux rope does not reconnect away from the AR since there is a very limited negative polarity magnetic flux around it. As a consequence, the flux rope remains line-tied at its positive footpoint. In contrast, the negative footpoint reconnects quickly and extensively with the positive magnetic flux, partly from the positive spot of AR 10798 and partly from the neighboring coronal hole. The reconnection is a two-phase process as illustrated in Figure 5. In the first phase (top panels), all of the twisted closed field lines of the flux rope (dark blue) reconnect with the streamer magnetic field (green). It results in erupting field lines connecting the positive footpoint of the flux rope with the streamer, shown in yellow and post-flare loops in fushia. In the second phase (bottom panels), the newly formed (yellow) erupting field lines reconnect with open field lines to form (orange) open and twisted erupting field lines. Below, we describe the detailed

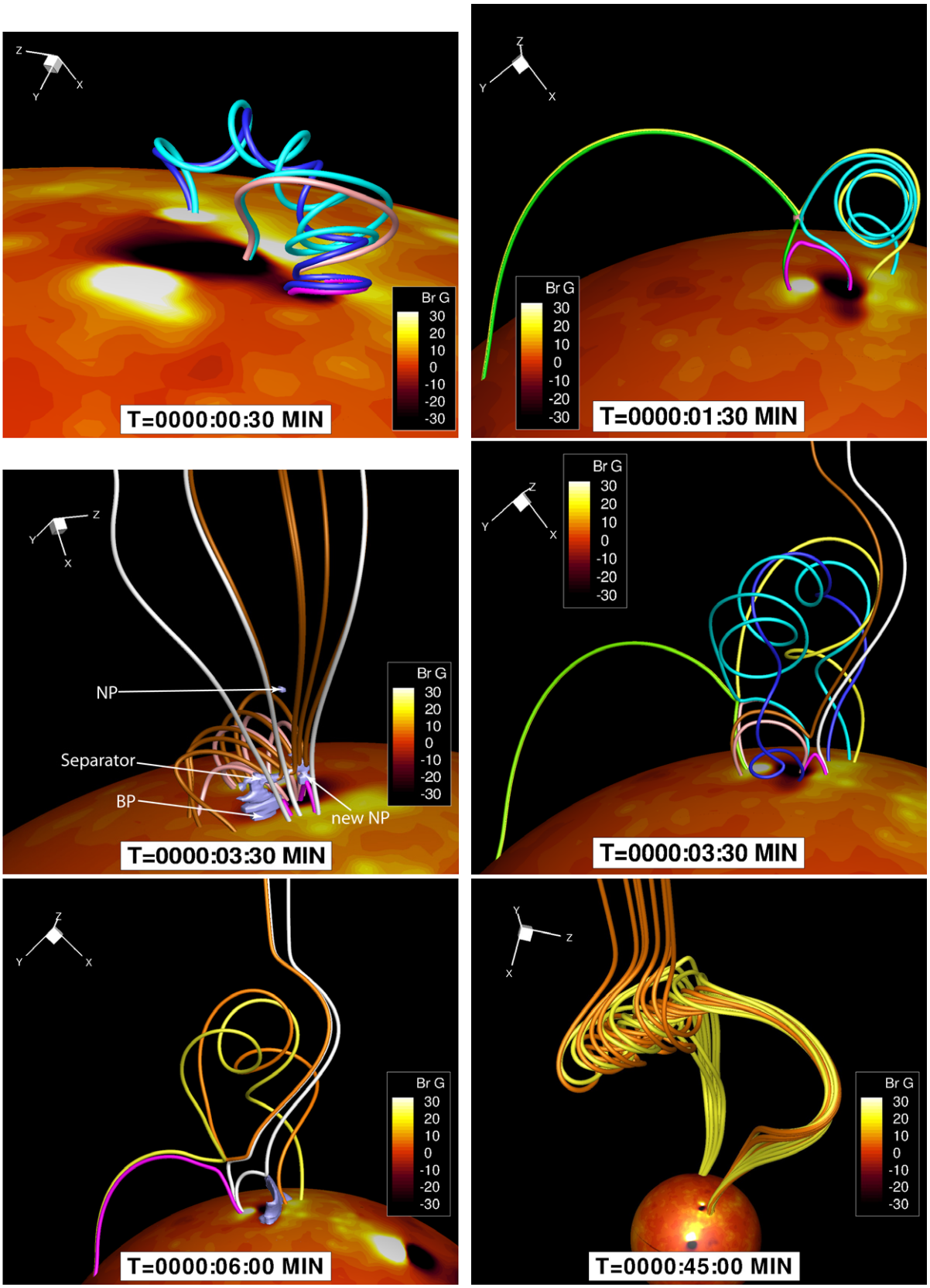

Figure 5. Reconnection process of the flux rope at time 0.5, 1.5, 3.5 (twice), 6, and 45 minutes after the superposition of the flux rope onto the solar corona. In all panels, the sphere is at 1.01 $R_{\odot}$ and is color-coded with the radial magnetic field strength. Dark blue, green, pink, and white field lines show the initial flux rope magnetic field, the streamer magnetic field, the anemone magnetic field, and open magnetic field, respectively. Light blue field lines are the result of the first step of the first phase of the reconnection process. Yellow and orange magnetic field lines are the result of the two-phase reconnection process. Yellow field lines are closed and connect the positive polarity spot of the AR to the streamer belt. Orange field lines are open. Fushia field lines are post-flare loops. In the middle panels, brown field lines are newly open. In the bottom right panel, there is an equal number of open and closed twisted field lines. See online movies for a different view.

(Animations (a and b) and a color version of this figure are available in the online journal.)

reconnection process and the change in magnetic topology during the eruption.

3.3. Details of the Reconnection Process and Changes in the Magnetic Topology

The reconnection involves two phases: the first one, when the negative footpoint of the flux rope reconnects outside the fan surface (top panels of Figure 5) and the second one, when some of the erupting field lines open up (bottom panels of Figure 5). The detailed reconnection process of this first phase goes as follows: first, the (dark blue) field lines of the flux rope reconnect with overlying anemone field (pink) to form twisted (light blue) field lines connecting the positive footpoint of the flux rope with the negative main spot of the AR (top left panel of Figure 5). This reconnection happens at the BP. In a second step, the newly formed field lines (light blue) reconnect with closed (green) field lines outside of the fan surface to form the (yellow) field lines connecting the positive footpoint of the flux rope with the streamer (top right panel). This reconnection occurs at the NP. The two steps of the first phase are nearly simultaneous and overlying closed field lines from the streamer belt flux system (green field lines) reconnect away.

During the reconnection process, an NP forms below the flux rope and there is a separator linking the BP and this NP. This separator is similar to the BP–BP separator or the quasi-separatrix layer discussed for example in Titov & Démoulin (1999) and Aulanier et al. (2010) and it is shown in metallic blue in the middle left panel of Figure 5. A current sheet forms in association with the separator and it is shown as a purple surface in the bottom left panel of Figure 5. The current sheet takes a sigmoidal shape, which is very common from flux emergence and shearing motions (Manchester et al. 2004a; Titov et al. 2008; Aulanier et al. 2010) but it can also be the result of reconnection with adjacent flux systems and due to the pre-event topology as is found here.

During the first phase, which lasts about 5–10 minutes, the flux rope expands to a height of 1 $R_\odot$ above the solar surface. Due to the CME expansion, the NP is pushed eastward along the outer spine by about 3° and its height increases by about 0.04 $R_\odot$. At the end of this phase, the flux rope remains composed of closed field lines but it appears totally disconnected from its original negative footpoint (see the top right panel of Figure 6).

Open field lines (white) from the leading positive spot reconnect at the separator below the flux rope with anemone field lines to form new open field lines (shown in brown) passing at proximity of the NP. Separator reconnection is described in Parnell & Galsgaard (2004), for example. This is illustrated in the middle left panel of Figure 5. A similar type of reconnection following the eruption of a flux rope has been previously discussed in Mackay & van Ballegooijen (2006). Due to the reconnection of the anemone flux system and the streamer belt and due to the formation of the separator, the magnetic topology changes quite drastically from the pre-event topology. The NP below the flux rope separates the anemone flux system and open field lines originating from the leading (white) and trailing (brown) positive spots (middle left panel of Figure 5). The outer spine of this system is open. Such an opening of a similar topology during a time-dependent process was shown in Edmondson et al. (2010). The eastern NP separates the erupting (yellow) magnetic field and the closed field originating from the positive trailing spot. The outer spine connects the positive trailing spot and the positive footpoint of the flux rope through the flux rope. The full magnetic topology with all the different types of field lines discussed here is shown in the middle right panel of Figure 5. The presence of two NPs separating different but overlapping flux systems, as shown here, is only possible in a fully three-dimensional simulation as is the case here. The second phase of reconnection happens when the flux rope is not connected anymore to the negative spot of AR 10798.

The second phase of the evolution starts when the negative footpoint of the flux rope has fully reconnected outside of the fan surface (light and dark blue field lines no longer exist). Then, the flux rope has raised, expanded, and deflected enough so that side reconnection happens with open magnetic field lines at the NP (similar to what was found in Chen & Shibata 2000). The reconnection of closed erupting field lines with open field lines from an equatorial coronal hole is a type of interchange reconnection. Here, contrary to the case described in Crooker et al. (2002), the open field lines are only transported over a very small distances as they reconnect with closed field lines, because the entire AR is surrounded by equatorial coronal holes. This special form of interchange reconnection is due to the anemone nature of the AR and one can expect that it happens in most eruptions from an AR inside a coronal hole. It has been previously discussed in an observational study of an eruption from an anemone AR on 2007 October 17 (Baker et al. 2009).

At the time the second phase of reconnection starts, about 6 minutes after the CME initiation, the apex of the flux rope is at 1 $R_\odot$ above the solar surface and the NP is only at a height of 0.2 $R_\odot$. In this phase (bottom panels of Figure 5), the yellow erupting field lines connecting the positive footpoint of the flux rope to the streamer reconnect with white open field lines to form open, twisted field lines (shown in orange color). During this phase, the NP rises and is pushed eastward. Its evolution as well as that of the apex of the flux rope is shown in the right panels of Figure 7. Note that at all time, the NP is below and to the east side of the flux rope. An online animation shows the first 10 minutes of the CME evolution with the two-phase reconnection.

3.4. Mix of Closed and Open Field and Dimming Regions

The end result of the reconnection described in the previous subsection is typically an opening of the flux rope magnetic field but it is a relatively complex process and, importantly, some of the magnetic field lines of the flux rope remain closed until the end of our simulation (see bottom right panels of Figures 5 and 6). As seen in the bottom right panel of Figure 5, at time $t = 45$ minutes, the CME is composed of a mix of closed (yellow) and open (orange) field lines. The closed field lines are highly twisted and they have, in general, one footpoint (positive polarity) near the source region of the CME and the other footpoint (negative polarity) in the quiet Sun due to reconnection with the streamer belt. The open field lines are also highly twisted because they are due to the reconnection of the magnetic field of the flux rope with that of the background originating from the coronal hole just southwest of AR 10798 (positive polarity). This picture is similar to the sketches of Gosling et al. (1995) with open plasmoid field lines embedded inside closed twisted field lines.

Figure 8 shows a base difference of the 195 Å image 95 minutes after the start of the eruption with a pre-event image for the simulation (left) and from EIT (middle). As highlighted in this figure, the presence of erupted field lines with a footprint at

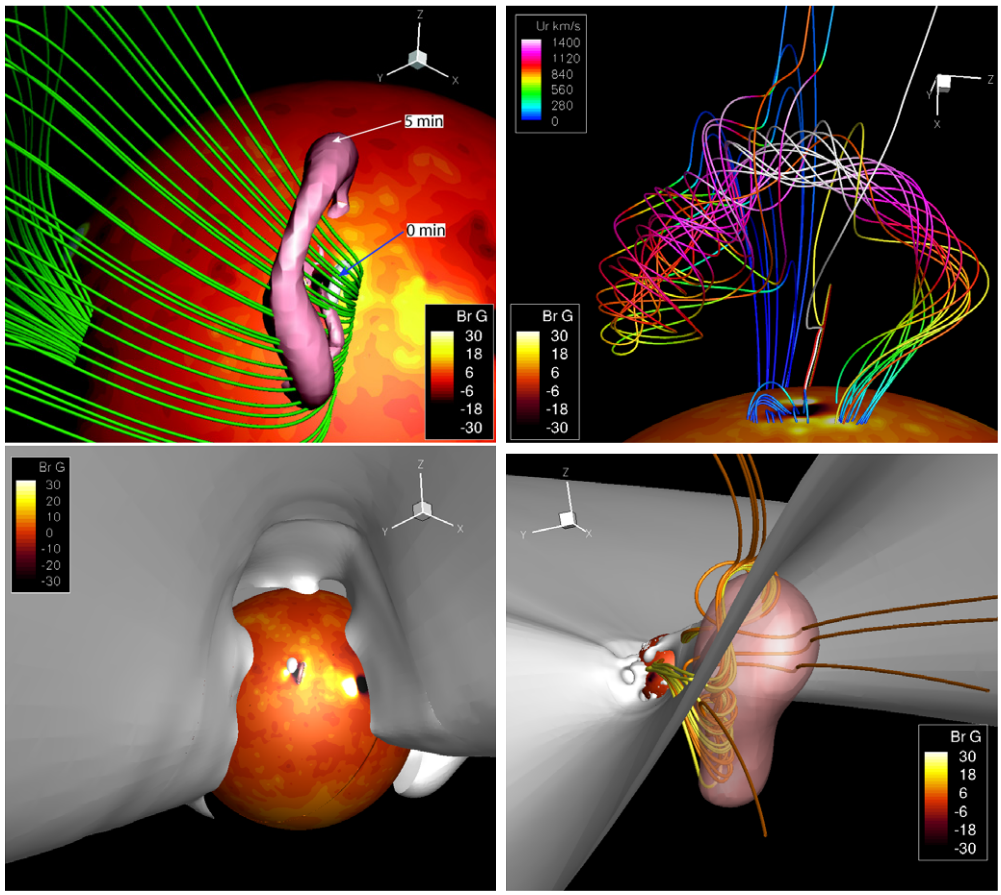

Figure 6. Top left panel: the pink surface is an isosurface of current density at time $t = 5$ minutes showing the deformation of the flux rope as compared to the initial flux tube shown as a white isosurface of current density. The green field lines belong to the streamer belt at time $t = 0$. Top right panel: magnetic field lines color-coded with the radial velocity 6 minutes after the superposition of the flux rope. This panel illustrates the state of the flux rope after the first phase of reconnection. Bottom left panel: initial orientation of the flux rope (pink isosurface) with respect to the current sheet (white isosurface). Bottom right panel: CME after 1 hr. The pink transparent surface is an isosurface of velocity equal to 800 km s^{-1} illustrating the position and orientation of the CME. The white surface is the current sheet (same as left panel). It illustrates how the CME is not aligned with the HCS as it leaves the corona. For the left panels, the view is approximately from the ecliptic plane above AR 10798. For the top right panel, the view is from the western limb looking at AR 10798. For the bottom right panel, the view is approximately from Earth.

(A color version of this figure is available in the online journal.)

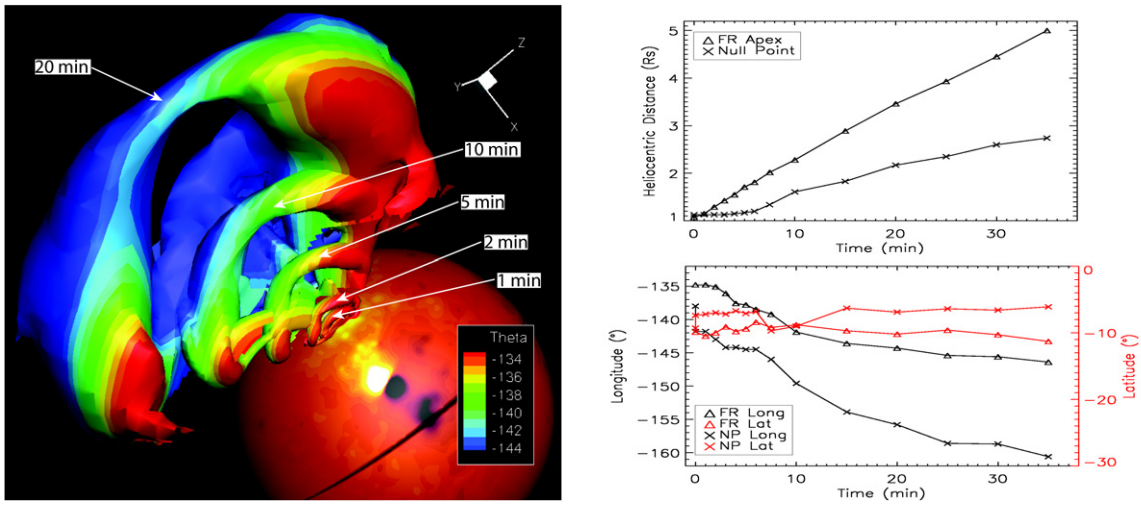

Figure 7. Left panel: five views of the flux rope at time 1, 2, 5, 10, and 20 minutes after the superposition of the flux rope onto the solar surface. Each surface is an isosurface of current density and they are color-coded with the longitude. As the color contour goes from dark red to dark blue, the longitude varies from 0 to 10° east of the location of the active region, illustrating the CME deflection. The initial longitude of the flux rope in the coordinate system of the figure is −134.5; after 20 minutes it is about −143°. This panel also illustrates how the CME is deformed but does not rotate. This view is from above the western limb looking down at AR 10798. Right panel: evolution of the apex of the flux rope and that of the pre-existing null point (top: distance; bottom: latitude, red and longitude, black).

(A color version of this figure is available in the online journal.)

Figure 8. EUV 195 Å base difference images of the CME showing the simulated corona at time $t = 95$ minutes (left) and an EIT image 94 minutes after the start of the HXR flare (middle) and about 7.5 hr later (right). In all images, the dimming region corresponding to the negative footpoint of the closed erupting field lines is highlighted by a white ellipse.

the edge of the streamer belt near disk center results in coronal dimmings from this region in our synthetic EUV images. These coronal dimmings were clearly visible in EIT images on the same region of the solar surface from about 01:26 UT on August 22 to the end of August 23. Dimming regions have been analyzed as the location of the footprint of the magnetic cloud (Webb et al. 2000; Mandrini et al. 2007) and/or the region where interchange reconnection happens (Attrill et al. 2006, 2007). Here, we find that the dimming region corresponds to the footprint of the magnetic cloud since erupting closed field lines have their negative footprint in this region. We believe that the appearance of the dimming region is only possible if the first phase of the reconnection process indeed happened as described in the previous section. It is hard to understand otherwise how the filament could reconnect with a distant region when reconnection with the adjacent coronal hole should happen preferentially.

Our simulation also shows how a flux rope originating from an AR inside a coronal hole can still contain closed field lines all the way to the outer corona (10 $R_\odot$). On 2005 August 24, ACE measured the passage of a small magnetic cloud, which has been associated with this eruption (Asai et al. 2009). While the smooth rotation only lasted for about 2 hr, it implies that twisted field lines associated with one of the two eruptions on August 22 made it to 1 AU. Figure 8 also includes a base difference image about 7.5 hr after the start of the eruption to illustrate the persistence of the dimming region. The dimming region was visible until the end of August 23 and it is likely that it persisted until around 12:00UT on August 24 but the observing geometry makes it hard to assess (the dimming region had moved close to the western limb of the Sun on August 24). The fact that dimming from the location of the negative footprints of the CME persisted until then would corroborate the measurement of a magnetic cloud at 1 AU at this time.

4. CME DEFLECTION, DEFORMATION, AND ROTATION

4.1. CME Deformation and Rotation

In the top right panel of Figure 6, we show the flux rope at time $t = 5$ minutes as a pink surface as well as the initial streamer field lines (green) and the initial flux rope position (white surface) corresponding to $t = 0$. From this figure, it is clear that the flux rope has been deformed from a straight tube into one with a sigmoid-like shape. The reason for the deformation is the reconnection with the streamer magnetic field lines (as discussed in the previous section). The reconnection happens at the negative footpoint of the flux rope (the one on the southern part of the sunspot) and it moves the footprints of the erupting field westward to the initial position of the streamer field lines, as is clear from this figure. The reconnection results in a rotation of the part of the flux rope which reconnects. It is similar to the rotation found in Cohen et al. (2010) but, here, we find that it only affects part of the CME. Also, the net result is not to align the CME with the current sheet but to deform it to make it a part of the CME aligned with the streamer belt. Because only part of the flux rope "rotates," it leads to a deformation, which makes the flux tube looks similar to a sigmoid with a marked skewness. This type of skewness has long been thought to be associated with shearing motions and it is produced by many CME initiation mechanisms involving shearing motions (Titov et al. 2008; Lynch et al. 2009; Amari et al. 2010; Aulanier et al. 2010) and flux emergence (Manchester et al. 2004a; Fan 2005). Here, we find that a straight flux rope may naturally develop a skewness as it interacts with the background magnetic field at a height as low as 0.7 $R_\odot$. This finding is in addition to the sigmoidal current sheet developing under the flux rope as discussed in Section 3.2.

We calculated the orientation of the central axis of the flux rope as it propagates from a distance of 1–8.5 $R_\odot$ (first hour) and we found no indication of rotation with an axis making an angle of $-15°$ to $-20°$ with the $-z$-axis. The bottom right panel of Figure 6 shows the CME after 1 hr as it has reached 8.5 $R_\odot$. The axis of the CME as illustrated by the magnetic field lines is found to be almost aligned with the initial axis of the flux rope. It is also illustrated in the first panel of Figure 7 with five views of the flux rope at different times from 1 to 20 minutes (corresponding to distances from 1 to 3.5 $R_\odot$). In this figure, the flux rope is plotted at different times as isosurfaces of current density. The color contours show the CME longitude. The angle between a given color and the CME axis gives an indication of the CME orientation. The angle is approximately constant over the 20 minutes covered by this figure, illustrating the lack of rotation. The magnetic field measurements at 1 AU (see Figure 9 of Asai et al. 2009) are consistent with a right-handed flux rope with a dominant southward axial component. It is the same as the orientation of the filament on the solar surface and, therefore, implies that there was no large-scale rotation during the CME propagation.

Lynch et al. (2009) proposed that the rotation of a CME in the corona is related to its skewness. It would be due to the force balance required to maintain this skewness which is lost as the CME erupts. It generates a torque created by the now unbalanced Lorentz force. However, here, the skewness is not the result of

shearing motions and it is not associated with force imbalance during the CME propagation. Therefore, our conclusion that the CME does not rotate is also consistent with this scenario. This result provides a caution on the association of skewness with CME rotation as it was found, here, that CME skewness can develop during the eruption, in which case no rotation is expected.

Cohen et al. (2010) found a strong rotation (∼90°) associated with the reconnection of a CME with the background magnetic field, yielding a CME whose axis is aligned with the HCS (as in Shiota et al. 2010). In our case, we found that only part of the flux rope reconnected, resulting in a deformation instead of a rotation of the flux rope axis. Although reconnection continues, it occurs primarily with open magnetic field lines, resulting in no change of the CME axis. Because there is no observational evidence that the CME rotated, it is important to understand why it is the case, when most recent simulations have had a tendency to show that CME rotation is a very frequent phenomena. Here, we find that the reconnection of one footprint of the CME results in a deformation of the CME but not a rotation and that the effect of the magnetic forces is to deflect the CME and not to rotate it (see the next section).

4.2. CME Deflection

Figure 7 illustrates the deflection of the flux rope. As shown in the right panels, the apex of the flux rope is found to deflect by about 10° in 35 minutes as it propagates to 5 $R_\odot$. After this time, the current inside the flux rope becomes so small that it is impossible to track the flux rope the same way as we did for the first 5 $R_\odot$. Instead, we track the position of the velocity disturbance associated with the CME. We find that the CME further deflects by about 1.°5 from $t = 35$ minutes to $t = 1$ hr, at what time the CME has reached 8.3 $R_\odot$. In the absence of a velocity shear in the solar wind which could "push" the CME away from the coronal holes, there are two possible causes for the deflection: (1) the side reconnection with the NP which happens at the east side of the CME and (2) the effect of the Lorentz force.

The flux rope is created by a southward line current and the global magnetic field above AR 10798 is of unipolar positive polarity. The Lorentz force acting on the flux rope is, therefore, almost purely eastward. The Lorentz force here is similar to that of the models of Chen (1996) and Isenberg & Forbes (2007) but in these studies, it results in acceleration and rotation, respectively, due to different magnetic topologies. Here, due to the largely unipolar polarity, the Lorentz force can deflect the CME. Side reconnection resulting in CME deflection can be seen in the work of Chen & Shibata (2000), for example. It is not straightforward to determine the cause of the CME deflection. However, during the first phase of the reconnection (first 6 minutes), the main part of the flux rope appears to be relatively unaffected by the reconnection as its negative footpoint reconnects (see the top left panel of Figure 7, for example). In addition, the reconnection is a breakout type reconnection (above the flux rope) and not a side reconnection. No deflection has yet been reported for asymmetric breakout simulations (e.g., see Lynch et al. 2009). In addition, the deflection rate of the NP does not correspond to that of the apex of the flux rope, as shown in the right panel of Figure 7. During the second phase of the reconnection, the side reconnection results in an opening of the magnetic field of the flux rope and it is unclear whether it affects or not the CME direction. For these reasons, we believe that it is likely that the Lorentz force is the main contributor to the deflection of the flux rope.

The Lorentz force is expected to decrease as the CME rises since both the magnetic field strength and the current decrease with height. We find that the deflection rate decreases with height and the CME only deflects by about 2° in the second 30 minutes of its propagation. It is consistent with the Lorentz force being the cause of the deflection. The deflection of the actual filament at the Sun could be greater than what is found in the simulation because its speed in the LC, where the Lorentz force is stronger, was certainly lower than that in our simulation. As noted above, the simulation does not reproduce the slow rise of the CME for the 18 minutes from the start of the SXR flare to the start of the HXR flare. It might create an additional deflection of about 5°–10° in the LC, assuming that the actual deflection rate is more or less consistent with what we find in our simulation. Another reason why our simulation does not reproduce the observed deflection is also due the initiation mechanism. As the force-free field of the flux rope is superimposed onto the coronal magnetic field, it results in a magnetic configuration which is not force-free. Therefore, there are additional Lorentz forces on all directions, which partially compensate the main eastward Lorentz force discussed before. In the real Sun, it is likely that the filament was in a force-free state before the eruption and it would only be subject to the main eastward Lorentz force, which would yield a larger deflection. Deflection of CMEs from the same AR during the following Carrington rotation has also been reported (Wang et al. 2006).

5. DISCUSSIONS AND CONCLUSION

We have investigated, using a numerical simulation, the first of two eruptions on 2005 August 22 from anemone AR 10798. We have used a recently developed component of the SWMF to include realistic thermodynamics into the representation of the LC. Using the LC component has enabled us to produce EUV images of the solar corona which we can compare to EIT observations. In addition, previous work have shown that including thermodynamics is important to reproduce the plasma and magnetic properties of the entire corona. We have investigated the pre-event topology of the AR and found that it indeed developed into an anemone AR with a single NP separating the AR flux system to unipolar positive magnetic field. We have found that some of these unipolar magnetic field lines are open while others are part of the streamer belt connected to a region near disk center. Pre-event 171 Å and 195 Å images of the corona are in good agreement with simulated ones, validating our steady-state model. In agreement with observations of an Hα filament, which was well observed prior to the eruption, we have superposed a highly twisted flux rope onto the steady-state solar corona at the same location and with the same orientation and chirality (right-handed and southward). Due to force imbalance, the flux rope immediately erupts and we have focused our study on its interaction with the adjacent magnetic flux systems and in particular with the open flux from the surrounding coronal holes.

The anemone nature of the source region has two major consequences on the evolution of the CME: an eastward deflection due to the Lorentz force and a reconnection of the negative footpoint of the flux rope, which results in the appearance of a long-duration dimming region and a mix of open and closed field lines in the CME. Since the flux rope was southward and right-handed, there was a strong southward axial current. The Lorentz force generated by this current and the unipolar

positive magnetic field in the vicinity of the AR is east-directed and, in our simulation, it deflects the CME by about 10°–15° as the CME propagates to 8 $R_\odot$. We have not addressed the reason why CMEs from anemone ARs tend to be fast CMEs (Liu 2007). It should be however noted that, in the simulation, the CME encounters closed field lines in the LC, so the magnetic topology cannot be fully responsible for the fast speed. It is therefore likely that the fast speed of CMEs from anemone ARs is at least partially due to the fact that the CME propagates into a low-density, fast solar wind, where the hydrodynamical drag is low (Cargill 2004).

The negative footpoint of the flux rope quickly reconnects with the positive field part of the streamer belt. It leads to a CME with one footpoint (the positive one) that is line-tied, and the second one which connects to a region of the Sun about 40° away from the AR. A dimming region was found to develop in the region of the second footpoint, both in simulated EUV images and in EIT images and to persist at the Sun for as much as a day after the eruption. Additionally, some of these closed field lines reconnect with open field from the equatorial coronal hole in a type of interchange reconnection previously discussed in Baker et al. (2009). It yields a mix of open and closed field lines in the erupting ejecta. While we have conducted our simulation only to 10 $R_\odot$, this type of mixed nature of the erupting field is expected from observations of periods of unidirectional strahl inside periods of bi-directional electrons as a magnetic cloud passes over a spacecraft (Gosling et al. 1995; Shodhan et al. 2000). To the best of our knowledge, this is the first time such a mixture is obtained from a numerical simulation of a real CME event. The fact that we obtain interchange reconnection in our simulation is not surprising, since it has been noted before that anemone ARs are the most suitable environment for interchange reconnection (Baker et al. 2009).

We have also found that the CME does not rotate as it propagates in the corona (up to a distance of 10 $R_\odot$). This result is found although there is large-scale reconnection, the CME axis is initially not aligned with the HCS and the flux rope deforms into a skewed tube at a distance of less than 1.7 $R_\odot$. It shows that the rotation of the CME axis is not a universal process and that some CMEs maintain their orientation in spite of large-scale reconnection. This result is a pendant to previous numerical studies (Lynch et al. 2009; Cohen et al. 2010; Shiota et al. 2010) which found that rotation happens when a CME is initially misaligned with the HCS, or when it is skewed. The deflection of the CME, the persistence of closed field lines into the inner heliosphere, and the lack of rotation are also consistent with the observation of a short magnetic cloud at 1 AU about 2 days after the first eruption. Asai et al. (2009) associated this magnetic cloud with the first of the two eruptions of 2005 August 22.

While our simulation captures some of the most important observational features of the CME, there are some discrepancies. In our simulation, the CME does appear to propagate along the same latitude as that of its source region (S11), while LASCO images show a CME propagating close to the ecliptic. One likely explanation is that only the northern part of the filament erupted (as reported in Asai et al. 2009). Our method to obtain an eruption is too simple to study partial filament eruption or to reproduce the exact dynamics and kinematics of the eruption at distances less than 3 $R_\odot$. Another difference between the simulation and the observations is the amount of deflection. In our simulation, the CME deflects by about 10° eastward whereas a total deflection of about 40°–50° is expected from observations. A smaller deflection might be present in our simulation compared to what happened on the real Sun because of different kinematics and force balance in the LC. However, we believe that a significant portion of the deflection cannot be accounted by magnetic forces, which are dominant in the LC. This finding implies that a significant part of the deflection is due to hydrodynamical effect. For this CME from an anemone AR, followed by a twice faster ejection 18 hr later, these effects may take two forms: deflection by the fast wind from the coronal hole as discussed, for example, in Wang et al. (2004) and Gopalswamy et al. (2009) and also deflection by the second, faster CME pushing the eruption from behind, as discussed in Xiong et al. (2009). In this case, the additional deflection can be expected to happen more gradually in the heliosphere. Future simulations will investigate the heliospheric evolution of CMEs from anemone ARs and overtaken by faster eruption.

The research for this manuscript was performed during and supported by a JSPS short-term post-doctoral fellowship at Kwasan Observatory in Kyoto University. We thank the reviewer and Terry Forbes for their helpful comments, which helped us clarify the discussion of the reconnection process. N.L. thanks everyone from the Kwasan Observatory for their welcome during his seven month stay there. N.L. and I.R. acknowledge additional financial support from NSF grants AGS0639335 and AGS0819653 and NASA grant NNX08AQ16G. C.D. was supported by a NASA NESSF08-Helio08F-0007.

REFERENCES

Altschuler, M. D., Levine, R. H., Stix, M., & Harvey, J. 1977, Sol. Phys., 51, 345
Amari, T., Aly, J., Mikic, Z., & Linker, J. 2010, ApJ, 717, L26
Asai, A., Shibata, K., Hara, H., & Nitta, N. V. 2008, ApJ, 673, 1188
Asai, A., Shibata, K., Ishii, T. T., et al. 2009, J. Geophys. Res., 114, A00A21
Attrill, G. D. R., Harra, L. K., van Driel-Gesztelyi, L., & Démoulin, P. 2007, ApJ, 656, L101
Attrill, G. D. R., Nakwacki, M. S., Harra, L. K., et al. 2006, Sol. Phys., 238, 117
Aulanier, G., Török, T., Démoulin, P., & DeLuca, E. E. 2010, ApJ, 708, 314
Baker, D., Rouillard, A. P., van Driel-Gesztelyi, L., et al. 2009, Ann. Geophys., 27, 3883
Byrne, J. P., Maloney, S. A., McAteer, R. T. J., Refojo, J. M., & Gallagher, P. T. 2010, Nat. Commun., 1, 74
Cargill, P. J. 2004, Sol. Phys., 221, 135
Chen, J. 1996, J. Geophys. Res., 101, 27499
Chen, P. F., & Shibata, K. 2000, ApJ, 545, 52
Chertok, I. M., Obridko, E. I., Mogilevsky, V. N., Shilova, N. S., & Hudson, H. S. 2002, ApJ, 567, 1225
Cohen, O., Attrill, G. D. R., Schwadron, N. A., et al. 2010, J. Geophys. Res., 115, A10104
Cohen, O., Sokolov, I. V., Roussev, I. I., et al. 2007, ApJ, 654, L163
Cremades, H., Bothmer, V., & Tripathi, D. 2006, Adv. Space Res., 38, 461
Crooker, N. U., Gosling, J. T., & Kahler, S. W. 2002, J. Geophys. Res., 107, 1028
Delaboudinière, J. P., Artzner, G. E., Brunaud, J., et al. 1995, Sol. Phys., 162, 291
Downs, C., Roussev, I. I., van der Holst, B., et al. 2010, ApJ, 712, 1219
Downs, C., Roussev, I. I., van der Holst, B., et al. 2011, ApJ, 728, 2
Edmondson, J. K., Antiochos, S. K., DeVore, C. R., Lynch, B. J., & Zurbuchen, T. H. 2010, ApJ, 714, 517
Evans, R. M., Opher, M., & Gombosi, T. I. 2011, ApJ, 728, 41
Fan, Y. 2005, ApJ, 630, 543
Filippov, B. P., Gopalswamy, N., & Lozhechkin, A. V. 2001, Sol. Phys., 203, 119
Forbes, T. G. 2000, J. Geophys. Res., 105, 23153
Gopalswamy, N., Mäkelä, P., Xie, H., Akiyama, S., & Yashiro, S. 2009, J. Geophys. Res., 114, A00A22
Gosling, J. T., Birn, J., & Hesse, M. 1995, Geophys. Res. Lett., 22, 869
Hale, G. E., Ellerman, F., Nicholson, S. B., & Joy, A. H. 1919, ApJ, 49, 153
Hill, S. M., Pizzo, V. J., Balch, C. C., et al. 2005, Sol. Phys., 226, 255
Isenberg, P. A., & Forbes, T. G. 2007, ApJ, 670, 1453

Jacobs, C., Roussev, I. I., Lugaz, N., & Poedts, S. 2009, ApJ, 695, L171
Kilpua, E. K. J., Liewer, P. C., Farrugia, C., et al. 2008, Sol. Phys., 254, 325
Lin, R. P., Dennis, B. R., Hurford, G. J., et al. 2002, Sol. Phys., 210, 3
Lionello, R., Linker, J. A., & Mikić, Z. 2001, ApJ, 546, 542
Lionello, R., Linker, J. A., & Mikić, Z. 2009, ApJ, 690, 902
Liu, Y. 2007, ApJ, 654, L171
Liu, Y., Thernisien, A., Luhmann, J. G., et al. 2010, ApJ, 722, 1762
Lugaz, N., Manchester, W. B., & Gombosi, T. I. 2005, ApJ, 634, 651
Lugaz, N., Manchester, W. B., Roussev, I. I., Tóth, G., & Gombosi, T. I. 2007, ApJ, 659, 788
Lugaz, N., Roussev, I. I., Sokolov, I. V., & Jacobs, C. 2010, in AIP Conf. Proc. 1216, 12th Int. Solar Wind Conf., ed. M. Maksimovic et al. (Melville, NY: AIP), 440
Lugaz, N., Vourlidas, A., Roussev, I. I., & Morgan, H. 2009, Sol. Phys., 256, 269
Lynch, B. J., Antiochos, S. K., Li, Y., Luhmann, J. G., & DeVore, C. R. 2009, ApJ, 697, 1918
Mackay, D. H., Karpen, J. T., Ballester, J. L., Schmieder, B., & Aulanier, G. 2010, Space Sci. Rev., 151, 333
Mackay, D. H., & van Ballegooijen, A. A. 2006, ApJ, 642, 1193
MacQueen, R. M., Hundhausen, A. J., & Conover, C. W. 1986, J. Geophys. Res., 91, 31
Manchester, W. B., Gombosi, T., DeZeeuw, D., & Fan, Y. 2004a, ApJ, 610, 588
Manchester, W. B., Gombosi, T. I., Roussev, I. I., et al. 2004b, J. Geophys. Res., 109, A01102
Mandrini, C. H., Nakwacki, M. S., Attrill, G., et al. 2007, Sol. Phys., 244, 25
Morgan, H., Habbal, S. R., & Woo, R. 2006, Sol. Phys., 236, 263
Ogawara, Y., Takano, T., Kato, T., et al. 1991, Sol. Phys., 136, 1
Ohyama, M., & Shibata, K. 1998, ApJ, 499, 934
Pariat, E., Antiochos, S. K., & DeVore, C. R. 2009, ApJ, 691, 61
Parnell, C. E., & Galsgaard, K. 2004, A&A, 428, 595
Plunkett, S. P., Thompson, B. J., St., Cyr, O. C., & Howard, R. A. 2001, J. Atmos. Sol.-Terr. Phys., 63, 389
Roussev, I. I., Forbes, T. G., Gombosi, T. I., et al. 2003, ApJ, 588, L45
Roussev, I. I., Lugaz, N., & Sokolov, I. V. 2007, ApJ, 668, L87
Sheeley, N. R., Jr, Bohlin, J. D., Brueckner, G. E., et al. 1975, Sol. Phys., 40, 103
Shen, C., Wang, Y., Gui, B., Ye, P., & Wang, S. 2011, Sol. Phys., 269, 389
Shibata, K., Nakamura, T., Matsumoto, T., et al. 2007, Science, 318, 1591
Shibata, K., Nitta, N., Strong, K. T., et al. 1994, ApJ, 431, L51
Shiota, D., Kusano, K., Miyoshi, T., & Shibata, K. 2010, ApJ, 718, 1305
Shodhan, S., Crooker, N. U., Kahler, S. W., et al. 2000, J. Geophys. Res., 105, 27261
Temmer, M., Veronig, A. M., Vršnak, B., et al. 2008, ApJ, 673, L95
Titov, V. S., & Démoulin, P. 1999, A&A, 351, 707
Titov, V. S., Mikic, Z., Linker, J. A., & Lionello, R. 2008, ApJ, 675, 1614
Török, T., & Kliem, B. 2003, A&A, 406, 1043
Tóth, G., Sokolov, I. V., Gombosi, T. I., et al. 2005, J. Geophys. Res., 110, A12226
Tóth, G., van der Holst, B., & Huang, Z. 2011, ApJ, 732, 102
Tsuneta, S., et al. 1991, Sol. Phys., 136, 37
van der Holst, B., Manchester, W. B., Frazin, R. A., et al. 2010, ApJ, 725, 1373
Vourlidas, A., Bastian, T. S., Nitta, N., & Aschwanden, M. J. 1996, Sol. Phys., 163, 99
Wang, Y., Shen, C., Wang, S., & Ye, P. 2004, Sol. Phys., 222, 329
Wang, Y., Xue, X., Shen, C., et al. 2006, ApJ, 646, 625
Webb, D. F., Lepping, R. P., Burlaga, L. F., et al. 2000, J. Geophys. Res., 105, 27251
Xiong, M., Zheng, H., & Wang, S. 2009, J. Geophys. Res., 114, A11101
Yurchyshyn, V. 2008, ApJ, 675, L49
Yurchyshyn, V., Abramenko, V., & Tripathi, D. 2009, ApJ, 705, 426